

**Accurate Magnitude and Stress Drop using the Spectral Ratios Method Applied to  
Distributed Acoustic Sensing**

**Itzhak Lior<sup>1</sup>**

<sup>1</sup>Institute of Earth Sciences, The Hebrew University, Jerusalem, Israel.

Corresponding author: Itzhak Lior (itzhak.lior@mail.huji.ac.il)

**Key Points:**

- The spectral ratios approach was applied to 9 earthquakes in Israel recorded by DAS and accelerometers
- Accurate relative magnitudes and stress drops were calculated
- DAS can provide reliable source parameter estimates that may outperform accelerometers

## Abstract

The reliable estimation of earthquake magnitude and stress drop are key in seismology. The novel technology of distributed acoustic sensing (DAS) holds great promise for source parameter inversion owing to the measurements' high spatial density. In this study, I demonstrate the robustness of DAS for magnitude and stress drop estimation using the empirical Green's function deconvolution method. This method is applied to 9 co-located earthquakes recorded in Israel following the 2023 Turkey earthquakes. Spectral ratios were stacked along the fiber, and fitted with a relative Boatwright source spectral model. Excellent fits were obtained even for similar sized earthquakes. Stable seismic moments and stress drops were calculated assuming the moment of one earthquake is known. DAS derived estimates were found to be more stable and reliable than those obtained using a dense accelerometer network. The results demonstrate the great potential of DAS for source studies.

## Plain Language Summary

Estimating earthquake magnitude and stress drop, the two most fundamental source parameters, is key for various seismological investigations, including earthquake self-similarity and hazard mitigation. The extraction of source parameters requires that source and path effects are reliably deconvolved from source contributions. One approach is to deconvolve a small earthquake from a co-located larger one in the frequency domain such that common path and site functions cancel and relative source function, between both earthquakes, remain. In this study, I apply the deconvolution approach to 9 earthquakes that followed the 2023 Turkey earthquakes, recorded using distributed acoustic sensing (DAS) applied to an optical fiber in Israel. DAS converts standard optical fibers into dense arrays, with seismic measurements every few meters along tens-of-kilometers long fibers. The deconvolution was calculated for different earthquake pairs and excellent fits were obtained with a relative source spectral model. Stable seismic moments and stress drops were calculated. These parameters were found to be more reliable than those obtained using a dense standard-accelerometer network. The results demonstrate the great potential of DAS for source studies.

## 1 Introduction

Estimating earthquake magnitudes and stress drops is fundamental for seismological research. Stress drop is key in studying earthquake self-similarity (e.g., Ide & Beroza, 2001) and strongly affects ground shaking intensity (e.g., Lior & Ziv, 2018). The estimation of these source parameters is model based, and achieved by isolating source contributions from path and site effects. Once the source term is extracted, it is fitted with a source model either in time (Al-Ismael et al., 2023; Lior & Ziv, 2018) or frequency (e.g., Huang et al., 2017; Lior & Ziv, 2017; Shearer et al., 2019) domains. The most commonly used model is the Omega-squared (Boatwright, 1980; Brune, 1970; Madariaga, 1976; Sato & Hirasawa, 1973), describing the far-field body-wave radiation. For ground displacement it reads as:

$$\Omega(f) = \frac{\Omega_0 U_{\phi\theta}}{\left[1 + \left(\frac{f}{f_0}\right)^{2\gamma}\right]^{1/\gamma}}, \quad (1)$$

where  $\gamma$  equals 1 (Brune, 1970) or 2 (Boatwright, 1980),  $f_0$  is the source corner frequency,  $\Omega_0$  is the low frequency displacement spectral plateau, and  $U_{\phi\theta}$  is the radiation pattern. The latter is a function of the focal mechanism, azimuth and take-off angle from the source (Aki & Richards,

2002; Kaneko & Shearer, 2015).  $\Omega_0$  is proportional to the seismic moment  $M_0$  divided by the hypocentral distance, and to parameters that describe the media (free surface amplification and density and velocity at the source). Stress drop is commonly estimated assuming a circular crack with uniform rupture velocity (Eshelby, 1957):

$$\Delta\tau = \frac{7}{16} M_0 \left( \frac{f_0}{kC_s} \right)^3, \quad (2)$$

where  $C_s$  is the shear-wave velocity and  $k$  is a phase dependent (P or S) model constant. Equations (1) and (2) describe a simple source model with a smooth, isotropic slip distribution on a circular patch.

Station-specific corner frequency and stress drop estimates exhibit large variability for the same earthquake (e.g., Abercrombie et al., 2017; Kaneko & Shearer, 2015; Lior & Ziv, 2018). These variabilities are mainly attributed to the improper extraction of source from path and site contributions, a hindrance that aggravates in the presence of low signal to noise ratio (SNR) conditions, i.e., for small earthquakes. In addition, since stress drops are the cube of corner frequencies (Equations 2), small errors in  $f_0$  translate to larger errors in  $\Delta\tau$ .

A common method for the reliable extraction of source contributions from path and site effects is the empirical Green's function (EGF), or spectral ratios, method. This method uses two co-located earthquakes recorded at the same location to deconvolve one from the other to remove common path, site and instrumental effects. The deconvolved spectra is then fitted with a relative source model to estimate the seismic moment ratio between both earthquakes, and the corner frequency of each earthquake (e.g., Abercrombie et al., 2017). This approach circumvents the modeling of path and site effects, overcoming the main difficulty in estimating source parameters.

However, the EGF method suffers from several drawbacks that reduce its performance and applicability. First, the magnitudes of both earthquakes need to be sufficiently different in order to reliably fit both corner frequencies. Typically, a magnitude difference of at least 1 unit is required (e.g., Abercrombie et al., 2017; Shearer et al., 2019). Second, while path and site effects are common for both earthquakes, noise conditions may not be, and spectral ratios need to be stacked to suppress random noise sources and facilitate reliable model fitting (e.g., Wu et al., 2019). Third, EGF analysis is only feasible in a limited frequency band where the spectral amplitudes of both earthquakes are above a predefined noise threshold, typically set to be 3 (e.g., Viegas et al., 2010). Using a too small frequency range may bias the fitted source parameters (Abercrombie, 2021). These requirements limit the applicability of this approach. The requirement that earthquakes be sufficiently different can be overcome by fitting for the low and high spectral plateaus in the relative spectra rather than the actual corner frequencies (Walter et al., 2017).

It has recently been demonstrated that the dense measurements of Distributed Acoustic Sensing (DAS) can be used to obtain spectral ratios (Chen, 2023). The use of DAS for source parameter estimation via the EGF method can overcome the previously described limitations of seismometer/accelerometer-based method. The application of the EGF method to DAS data is described in Text S1, with the conclusion that DAS strain (rate) data can be directly used to obtain spectral ratios (Equation S3):

$$\frac{\dot{\epsilon}_{ij}^e(f)}{\dot{\epsilon}_{2j}^e(f)} = \frac{M_{01} \left[ 1 + \left( \frac{f}{f_{02}} \right)^{2\gamma} \right]^{1/\gamma}}{M_{02} \left[ 1 + \left( \frac{f}{f_{01}} \right)^{2\gamma} \right]^{1/\gamma}}. \quad (3)$$

In this equation,  $\dot{\epsilon}_{ij}^e(f)$  are strain-rates of earthquake  $i$  ( $i = 1, 2$ ) recorded at DAS channel  $j$ , and  $M_{0i}$  and  $f_{0i}$  are earthquake-specific seismic moments and corner frequencies, respectively.

In this work, I demonstrate that high fidelity relative seismic moments, corner frequencies and relative stress drops can be obtained using DAS via the EGF method. For each earthquake, channel-specific S-wave spectral ratios were stacked along the entire fiber, and analyzed in the framework of Equation (3). The results were compared to those obtained using accelerometers.

This manuscript is organized as follows. First, I describe the DAS data and processing. Then, I demonstrate the method using 9 well-recorded co-located earthquakes that occurred in central Israel following the devastating 2023 Kahramanmaraş Mw7.8 and Mw7.6 Eastern Turkey earthquakes. Finally, I discuss implications for earthquake source studies.

## 2 Data and Preprocessing

Following the catastrophic 2023 Kahramanmaraş earthquake pair, Israel experienced a rapid increase in seismicity, including several earthquake clusters that occurred off the main Dead-Sea-Transform fault (Inbal et al., 2023). Here, I focus on one of these clusters of co-located earthquakes recorded by a nearby optical fiber and the dense Israeli Seismic Network (Kurzon et al., 2020) between February 7th and March 7th. Earthquakes, fiber and accelerometer location are shown in Figure 1a. During this period, 10 earthquakes magnitudes 2.5 to 3.4 were recorded and cataloged by the Geological Survey of Israel (Table S1).

DAS earthquake data were acquired using a Prisma Photonics interrogator unit. The system is harnessing an innovative Hyper-Scan technology to produce high-quality quantitative longitudinal strain-rate measurement. Measurements were made using a 34 km long fiber installed in central Israel (Figure 1a) with a gauge length of 18.2 m, spatial sampling of 9.1 m and sampling rate of 1500 Hz. Data were then resampled to 100 Hz.

In order to verify that the earthquakes qualify as EGF pairs, cross correlations (CC) were calculated using the nearest seismic station. Because I use a horizontal fiber, with reduced P-wave sensitivity (e.g., Papp et al., 2017), the analysis focuses only on S-waves. Horizontal acceleration time-series were low pass filtered at 5 Hz and CC were calculated in a 1 second window starting at the direct S-wave arrival at station MEFR (Figure 1a), located 10 km from the epicenter of the largest earthquake. Filtered time-series and CC values with respect to the largest earthquake are shown in Figure 1b. All CC values for both horizontal components were above 0.8, indicating significant similarity between the different earthquakes. Waveform similarity is also evident in the DAS recordings shown in Figure 1c. Similar features can be observed between the different earthquakes, for example, the coherent arrivals at the first kilometer and first half a second. In addition, similar CC values were observed for many DAS channels as further described. Thus, it is assumed that these earthquakes have a similar radiation pattern.

To obtain stacked spectral ratios, a few processing procedures were applied. First, DAS and horizontal accelerometer waveforms were aligned by calculating CC between the largest earthquake and each other event using a 3 seconds data interval starting 1 second before the

theoretical S-wave arrival. The theoretical S-wave arrivals are calculated for all events using the location of the largest earthquake (Mw3.4) (See Open Research). Tens of DAS and accelerometer channels produced CC values above 0.9 for all earthquakes. For DAS, the time shifts from this analysis are independent of the distance along the fiber, suggesting that these events are co-located. To focus on direct S-waves, I use a uniform data interval of 10 seconds for all earthquakes, starting 1 second before the S-wave arrival. DAS and accelerometer spectra are calculated using the multitaper approach with a time-bandwidth product of 3.5 and 6 Slepian tapers (Prieto, 2022). I then calculate frequency specific SNR using the spectra of the signal and pre-signal noise. The latter is calculated in an equivalent 10 second window. For each earthquake pair, at each channel along the fiber or horizontal accelerometer component, only frequencies with  $\text{SNR} > 1.5$  are considered; channel specific spectral ratios are calculated at these frequencies, and stacked. High SNR spectral ratio stacks were calculated separately for DAS (along the fiber) and accelerometers (using all stations with hypocentral distances below 100 km) for all possible earthquake pairs. Overall, up to 3689 DAS channels and 124 horizontal accelerometer components (62 stations) were used. Further analysis is conducted between 2 and 20 Hz, a bandwidth that includes the expected corner frequencies of all analyzed earthquakes.

### 3 Spectral Ratios Application to DAS Data

The stacked spectral ratios are resampled in equal log-of-frequency bins (e.g., Lior & Ziv, 2017) and their logarithms are fitted with the logarithm of Equation (3) to obtain the best fitting  $\log(M_{01}/M_{02})$ ,  $f_{01}$  and  $f_{02}$  estimates. Model fitting and parameter uncertainty estimation is similar to that proposed by Viegas et al. (2010). The inversion was done using a non-linear least square approach, implemented via Python's `curve_fit` tool. Parameter uncertainties were estimated by varying the value of one parameter and calculating the standard deviation of the fit while treating the other parameters as free fitting coefficients. The parameter-specific uncertainty range is determined by a standard deviation increase of 5%.

I calculate model fits to all DAS and accelerometer EGF pairs. DAS fits are shown in Figures 2 and S1 using the Boatwright ( $\gamma = 2$  in Equation 3) and Brune ( $\gamma = 1$  in Equation 3) models, respectively. Fits are quantified using the standard deviation ( $\sigma$ ) and  $R^2$ , (panel legends), and corner frequency uncertainties (error bars). In Figure 2, Only fits with  $\sigma \leq 0.05$ ,  $R^2 \geq 0.95$  and  $\log(M_{01}/M_{02}) \geq 0.5$  are considered; the former two disqualify suboptimal fits and the latter ensures earthquake magnitudes differ by at least 0.33 units. These conditions disqualify all pairs that include earthquake #8 (Table S1), whose recordings are contaminated by the coda of a larger earthquake. For easy comparison between the different models, the same spectral ratios are shown in both Figures 2 and S1. The Boatwright model (Figures 2), with sharper corner frequencies, clearly outperforms the Brune model (Figure S1), producing robust fits, lower parameter uncertainties, and consistent (within error bars) corner frequencies. Thus, the Boatwright model is used in following analysis.

Uncertainties in  $\log(M_{01}/M_{02})$  and  $\log(f_0)$  estimates are shown in Figure S2 for the fits in Figure 2. The observed uncertainties are small for all  $\log(f_0)$  (bounded at 0.05) and  $\log(M_{01}/M_{02})$  (bounded at 0.086), further demonstrating the reliability of the estimates. Furthermore, no clear correlation appears between  $\log(f_0)$  and  $\log(M_{01}/M_{02})$  estimates. This analysis demonstrates the reliability and robustness of the presented approach applied to DAS data.

A comparison between DAS and accelerometers, shown in Figures S3 and 3, reveals that the different instruments yield similar quality fits to the model, although parameters often vary significantly. Figure S3 shows a comparison between a DAS channel (#2339) and an accelerometer (station SLTI) located at a similar source-to-station azimuth, i.e., similar positions on the focal sphere (similar radiation patterns). Fitting quality ( $\sigma$  and  $R^2$ ) and parameters (figure caption) are similar. However, when spectral ratios are stacked over different source-station azimuths, significantly different parameters are often observed, as seen in Figure 3. This plot shows example spectral ratios for DAS (red) and accelerometers (blue), stacked over source-to-station azimuths of  $45^\circ$  and  $360^\circ$ , respectively. Excellent fits are obtained for both instruments but parameter values often differ substantially, with extreme examples such as the  $\log(M_{01}/M_{02})$  disparity in panel e (1.28 and 2.12 for DAS and accelerometers, respectively). Furthermore, accelerometer fits often indicate unrealistically high corner frequencies, at the edge of the frequency band (panels a and e). Unfortunately, most accelerometers are deployed east of the earthquakes, along the Dead-Sea-Fault, such that a reliable accelerometer stacked spectral ratios cannot be obtained in the equivalent DAS azimuthal aperture. In addition to the different azimuthal coverage for DAS and accelerometers, the disagreement between the spectral ratios in Figure 3 may stem from the different components used: only inline components for DAS and two orthogonal components for accelerometers.

#### 4 Implications for Source Parameter Studies

The spectral ratios method produces accurate corner frequencies, but only relative seismic moments; for accurate stress drops, reliable moment estimations are needed (Equation 2). The obtained results are unique in that each of the 9 earthquakes is used in different EGF pairs, with several corner frequency and relative moment estimates per earthquake; all moments may be estimated if one is known. Here, seismic moments are determined using a linear least-squares inversion, detailed in Text S2, where the magnitude of the largest earthquake is fixed to its catalog value of 4.3 (Table S1). The inversion produced stable earthquake specific seismic moments (Figure S4). Stress drops were then estimated via Equation 2 using the different corner frequencies,  $k = 0.21$  (Madariaga, 1976) and  $C_s = 3.2$  km/s (Nof et al., 2021). Event averaged source parameters are listed in Table S1. Figure 4 plots corner frequencies (panel a) and stress drops (panel b) as functions of earthquake-specific seismic moments. For comparison, the same procedure is applied to accelerometer data (Figure S5). It is evident that DAS derived  $f_0$  and  $\Delta\tau$  estimates are more stable and consistent than those obtained using accelerometers: the former exhibit smaller variabilities and a smaller range of  $\Delta\tau$  estimates.

Although small for all earthquakes, DAS derived corner frequency and stress drop variabilities are larger for the 3 largest earthquakes compared to the 6 smallest ones (Figure 4). This observation may be related to the prominent hump in the spectral ratio involving events #1 and #2, between the low frequency asymptote and the lower corner frequency (Figure 2), also observed for accelerometer data (Figure 3). To understand this observation, I examined the strain-rate amplitude spectra, corrected for hypocentral distances and stacked using high SNR amplitudes (Figure S6). The observed hump in Figure 2 is generated by a trough in the spectra of earthquakes #3 to #10 between 4 and 8 Hz. This trough is a deviation from the smooth omega-squared model, and suggests the presence of source complexities in these small earthquakes. Furthermore, the high frequency ( $>8$ Hz) spectra of events #6 and #10 (red curves in Figure S6) is unusually high for these weak events, possibly a result of increased anthropogenic noise near the fiber during daytime (Table S1). Thus, the smaller earthquakes do not perform as ideal Green's

functions when used with events #1 and #2, resulting in increased scatter. In contrast, the corner frequencies of the smaller earthquakes show remarkable consistency (Figures 2, 4 and S2) when using the different larger earthquakes. It should be noted that even the larger corner frequency variability is low: limited to  $\sim 0.2$  orders of magnitude.

While the linear fits in Figure 4, indicate that stress drop is magnitude invariant (self-similar), stress drop uncertainties and the limited magnitude range do not provide statistically meaningful observations; Additional smaller and larger earthquakes are required. For the studied earthquakes, stress drop has an average value of 37.6 MPa using the Madariaga (1976)  $k = 0.21$  parameters, or 6.88 MPa using the Brune (1970)  $k = 0.37$  parameter. These values depend on the magnitude used to constrain the least-squares inversion.

## 5 Conclusions

In this work, I demonstrated the robustness of DAS for source parameter estimation via the spectral ratios method applied to 9 co-located earthquakes in central Israel. Stacking high SNR spectral ratios produces smooth and coherent estimates that allow for the application of the EGF method even for similar sized earthquakes. I calculated spectral ratios for different earthquake pairs, and obtained excellent fits to the model with robust and stable estimates of seismic moment ratios and both corner frequencies. Fits obtained using the Boatwright model (Figure 2) significantly outperform those obtained using the Brune model (Figure S3). Having prior knowledge of one earthquake's moment magnitude, I performed a linear least-squares inversion to obtain earthquake specific seismic moments and stress drop.

The comparison between DAS and accelerometers shows that differences in the azimuthal aperture result in significantly different source parameters, even when model fits are of similar quality. It is expected that observed source parameters vary with source-to-station azimuth (e.g., Kaneko & Shearer, 2015), yielding different results for DAS and accelerometers. However, since  $f_0$  and  $\Delta\tau$  estimates in Figures 4 and S5 are already azimuthally averaged, they are expected to be consistent for each earthquake. For the current dataset, acceleration-derived results (Figure S5) exhibit larger scatter compared with DAS-derived results (Figures 4), suggesting that the latter are more reliable. Thus, the results in Figure S5b that may imply stress drop increase with seismic moment are considered unreliable. However, given the small number of observations, additional research and comparison between the different measurements is needed.

This application of the spectral ratios method assumes that DAS data displays a linear response (Equation S2). While several studies concluded that DAS amplitude and phase response are flat in a broad frequency range (Lindsey et al., 2020; Paitz et al., 2020), there may be other effects that can bias the deconvolution, including non-linear response to strong ground shaking in terms of coupling and optical effects, and erroneous phase-unwrapping (phase skipping). While these effects were not observed for the low strain-rates investigated here, they should be accounted for when analyzing high strain-rate amplitudes.

The results demonstrate the great potential of DAS for earthquake source studies: 1) Owing to the density of DAS measurements, stacked along the fiber, SNR requirements were reduced to  $\text{SNR} > 1.5$ , allowing for less restrictive application of the EGF method, especially beneficial for small earthquakes. Furthermore, having additional possible earthquake pairs for the same dataset, improves the stability of source parameter inversion. 2) Stacked spectral ratios

exhibit excellent fits to the model and small parameter variabilities, potentially facilitating investigations of azimuthal source parameter variations and complexities. This property may also allow for better separation of source from path and site effects. 3) The EGF method applied to DAS circumvents the need to convert DAS measurements to ground motions for source parameter inversion (Lior et al., 2021, 2023; Trabattoni et al., 2023). Finally, DAS can improve our knowledge of the relation between source parameters and ground motion variabilities, as well as our understanding of source complexities and self-similarity in various sized earthquakes.

## Acknowledgments

The author thanks Prisma Photonics for their extensive help and support in data acquisition, handling and transfer. The author thanks Bill Ellsworth and an anonymous reviewer for their very constructive remarks which significantly improved this manuscript.

## Open Research

Data to reproduce the results is found in Lior (2023). Focal solution for the Mw3.4 earthquake is available at [https://eq.gsi.gov.il/events/202302072113/MT/2023-02-07T21.14.28\\_d12\\_GitHDUF05.pdf](https://eq.gsi.gov.il/events/202302072113/MT/2023-02-07T21.14.28_d12_GitHDUF05.pdf)

## References

- Abercrombie, R. E. (2021). Resolution and uncertainties in estimates of earthquake stress drop and energy release. *Philosophical Transactions of the Royal Society A: Mathematical, Physical and Engineering Sciences*, 379(2196), 20200131.  
<https://doi.org/10.1098/rsta.2020.0131>
- Abercrombie, R. E., Bannister, S., Ristau, J., & Doser, D. (2017). Variability of earthquake stress drop in a subduction setting, the Hikurangi Margin, New Zealand. *Geophysical Journal International*, 208(1), 306–320. <https://doi.org/10.1093/gji/ggw393>
- Aki, K., & Richards, P. G. (2002). *Quantitative seismology* (2nd ed). University Science Books.
- Al-Ismail, F., Ellsworth, W. L., & Beroza, G. C. (2023). A Time-Domain Approach for Accurate Spectral Source Estimation with Application to Ridgecrest, California, Earthquakes. *Bulletin of the Seismological Society of America*, 113(3), 1091–1101.  
<https://doi.org/10.1785/0120220228>
- Boatwright, J. (1980). A spectral theory for circular seismic sources; simple estimates of source dimension, dynamic stress drop, and radiated seismic energy. *Bulletin of the*



*Seismological Society of America*, 70(1), 1–27.

<https://doi.org/10.1785/BSSA0700010001>

Brune, J. N. (1970). Tectonic stress and the spectra of seismic shear waves from earthquakes.

*Journal of Geophysical Research*, 75(26), 4997–5009.

<https://doi.org/10.1029/JB075i026p04997>

Chen, X. (2023). Source parameter analysis using distributed acoustic sensing – an example with the PoroTomo array. *Geophysical Journal International*, 233(3), 2207–2213.

<https://doi.org/10.1093/gji/ggad061>

Eshelby, J. D. (1957). The determination of the elastic field of an ellipsoidal inclusion, and related problems. *Proceedings of the Royal Society of London. Series A. Mathematical and Physical Sciences*, 241(1226), 376–396. <https://doi.org/10.1098/rspa.1957.0133>

Huang, Y., Ellsworth, W. L., & Beroza, G. C. (2017). Stress drops of induced and tectonic earthquakes in the central United States are indistinguishable. *Science Advances*, 3(8), e1700772. <https://doi.org/10.1126/sciadv.1700772>

Ide, S., & Beroza, G. C. (2001). Does apparent stress vary with earthquake size? *Geophysical Research Letters*, 28(17), 3349–3352. <https://doi.org/10.1029/2001GL013106>

Inbal, A., Ziv, A., Lior, I., Nof, R. N., & Eisermann, A. S. (2023). Non-Triggering and Then Triggering of a Repeating Aftershock Sequence in the Dead Sea by the 2023 Kahramanmaraş Earthquake Pair: Implications for the Physics of Remote Delayed Aftershocks. *Geophysical Research Letters*, 50(18), e2023GL104908.

<https://doi.org/10.1029/2023GL104908>

Kaneko, Y., & Shearer, P. M. (2015). Variability of seismic source spectra, estimated stress drop, and radiated energy, derived from cohesive-zone models of symmetrical and

- asymmetrical circular and elliptical ruptures. *Journal of Geophysical Research: Solid Earth*, 120(2), 1053–1079. <https://doi.org/10.1002/2014JB011642>
- Kurzon, I., Nof, R. N., Laporte, M., Lutzky, H., Polozov, A., Zakosky, D., Shulman, H., Goldenberg, A., Tatham, B., & Hamiel, Y. (2020). The “TRUAA” Seismic Network: Upgrading the Israel Seismic Network—Toward National Earthquake Early Warning System. *Seismological Research Letters*, 91(6), 3236–3255. <https://doi.org/10.1785/0220200169>
- Lindsey, N. J., Rademacher, H., & Ajo-Franklin, J. B. (2020). On the Broadband Instrument Response of Fiber-Optic DAS Arrays. *Journal of Geophysical Research: Solid Earth*, 125(2). <https://doi.org/10.1029/2019JB018145>
- Lior, I. (2023). Empirical Green’s Function applied to DAS [Dataset]. <https://osf.io/y8csp/>
- Lior, I., Rivet, D., Ampuero, J.-P., Sladen, A., Barrientos, S., Sánchez-Olavarria, R., Villarroel Opazo, G. A., & Bustamante Prado, J. A. (2023). Magnitude estimation and ground motion prediction to harness fiber optic distributed acoustic sensing for earthquake early warning. *Scientific Reports*, 13(1), Article 1. <https://doi.org/10.1038/s41598-023-27444-3>
- Lior, I., Sladen, A., Mercerat, D., Ampuero, J.-P., Rivet, D., & Sambolian, S. (2021). Strain to ground motion conversion of distributed acoustic sensing data for earthquake magnitude and stress drop determination. *Solid Earth*, 12(6), 1421–1442. <https://doi.org/10.5194/se-12-1421-2021>
- Lior, I., & Ziv, A. (2017). The Relation between Ground Acceleration and Earthquake Source Parameters: Theory and Observations. *Bulletin of the Seismological Society of America*, 107(2), 1012–1018. <https://doi.org/10.1785/0120160251>

- 336 Lior, I., & Ziv, A. (2018). The Relation Between Ground Motion, Earthquake Source  
337 Parameters, and Attenuation: Implications for Source Parameter Inversion and Ground  
338 Motion Prediction Equations. *Journal of Geophysical Research: Solid Earth*, 123(7),  
339 5886–5901. <https://doi.org/10.1029/2018JB015504>
- 340 Madariaga, R. (1976). Dynamics of an expanding circular fault. *Bulletin of the Seismological*  
341 *Society of America*, 66(3), 639–666.
- 342 Mateeva, A., Lopez, J., Potters, H., Mestayer, J., Cox, B., Kiyashchenko, D., Wills, P., Grandi,  
343 S., Hornman, K., Kuvshinov, B., Berlang, W., Yang, Z., & Detomo, R. (2014).  
344 Distributed acoustic sensing for reservoir monitoring with vertical seismic profiling:  
345 Distributed acoustic sensing (DAS) for reservoir monitoring with VSP. *Geophysical*  
346 *Prospecting*, 62(4), 679–692. <https://doi.org/10.1111/1365-2478.12116>
- 347 Nof, R. N., Lior, I., & Kurzon, I. (2021). Earthquake Early Warning System in Israel—Towards  
348 an Operational Stage. *Frontiers in Earth Science*, 9.  
349 <https://doi.org/10.3389/feart.2021.684421>
- 350 Paitz, P., Edme, P., Gräff, D., Walter, F., Doetsch, J., Chalari, A., Schmelzbach, C., & Fichtner,  
351 A. (2020). Empirical Investigations of the Instrument Response for Distributed Acoustic  
352 Sensing (DAS) across 17 Octaves. *Bulletin of the Seismological Society of America*.  
353 <https://doi.org/10.1785/0120200185>
- 354 Papp, B., Donno, D., Martin, J. E., & Hartog, A. H. (2017). A study of the geophysical response  
355 of distributed fibre optic acoustic sensors through laboratory-scale experiments:  
356 Geophysical response of fibre optic sensors. *Geophysical Prospecting*, 65(5), 1186–1204.  
357 <https://doi.org/10.1111/1365-2478.12471>

- Prieto, G. A. (2022). The *Multitaper* Spectrum Analysis Package in Python. *Seismological Research Letters*, 93(3), 1922–1929. <https://doi.org/10.1785/0220210332>
- Sato, T., & Hirasawa, T. (1973). Body wave spectra from propagating shear cracks. *Journal of Physics of the Earth*, 21(4), 415–431. <https://doi.org/10.4294/jpe1952.21.415>
- Sharon, M., Sagy, A., Kurzon, I., Marco, S., & Rosensaft, M. (2020). Assessment of seismic sources and capable faults through hierarchic tectonic criteria: Implications for seismic hazard in the Levant. *Natural Hazards and Earth System Sciences*, 20(1), 125–148. <https://doi.org/10.5194/nhess-20-125-2020>
- Shearer, P. M., Abercrombie, R. E., Trugman, D. T., & Wang, W. (2019). Comparing EGF Methods for Estimating Corner Frequency and Stress Drop From *P* Wave Spectra. *Journal of Geophysical Research: Solid Earth*, 124(4), 3966–3986. <https://doi.org/10.1029/2018JB016957>
- Trabattoni, A., Biagioli, F., Strumia, C., Ende, M. van den, Uccio, F. S. di, Festa, G., Rivet, D., Sladen, A., Ampuero, J. P., Metaxian, J. P., & Stutzmann, E. (2023). *From strain to displacement: Using deformation to enhance distributed acoustic sensing applications*. <https://eartharxiv.org/repository/view/5292/>
- Viegas, G., Abercrombie, R. E., & Kim, W.-Y. (2010). The 2002 M5 Au Sable Forks, NY, earthquake sequence: Source scaling relationships and energy budget. *Journal of Geophysical Research: Solid Earth*, 115(B7). <https://doi.org/10.1029/2009JB006799>
- Walter, W. R., Yoo, S.-H., Mayeda, K., & Gök, R. (2017). Earthquake stress via event ratio levels: Application to the 2011 and 2016 Oklahoma seismic sequences. *Geophysical Research Letters*, 44(7), 3147–3155. <https://doi.org/10.1002/2016GL072348>

Wu, Q., Chen, X., & Abercrombie, R. E. (2019). Source Complexity of the 2015 Mw 4.0

Guthrie, Oklahoma Earthquake. *Geophysical Research Letters*, 46(9), 4674–4684.

<https://doi.org/10.1029/2019GL082690>

## Figure Captions

**Figure 1.** (a) Map of catalog earthquake location (black star), seismometer (green triangles), fiber (red curve) and faults (black curves, from Sharon et al., 2020). The region is indicated by a black rectangle in the inset map. (b) The first second of the S-waves recorded by the north component of MEFR accelerometer are shown for all earthquakes. Earthquake numbers and magnitude (vertical axis) correspond to Table S1. Waveforms are normalized and vertically shifted for visibility. CC values for each waveform and the top one are indicated. (c) DAS S-wave recordings showing the first 3 seconds on a 2.2 km fiber segment. Each earthquake is normalized by its standard deviation. Earthquake number and magnitudes (Table S1) are reported in each panel.

**Figure 2.** Spectral ratios and fits using the Boatwright ( $\gamma = 2$  in Equation 3) model for different earthquake pairs. Stacked spectral ratios, resampled ratios and model fits are indicated by thin grey curves, black curves, and dashed colored curves, respectively. Standard deviations and  $R^2$  are indicated in the panel legends, horizontal error bars correspond to corner frequency uncertainties. Red, blue and magenta curves correspond to different larger earthquake while each panel shows a specific smaller earthquake. Earthquake magnitude and numbers (Table S1) are indicated in each curve.

**Figure 3.** A comparison between several DAS and accelerometer spectral ratios for the Boatwright ( $\gamma = 2$  in Equation 3) model. Stacked spectral ratios, resampled ratios and model fits are indicated by thin curves, thick curves, and dashed curves, respectively. Standard deviations and  $R^2$  are indicated in the panel legends, horizontal error bars correspond to corner frequency uncertainties. Red and blue curves correspond to DAS and accelerometer spectral ratios, respectively. Earthquake magnitude and numbers (Table S1) are indicated in each panel.

**Figure 4.** The logarithms of (a) corner frequencies and (b) stress drops as functions of the logarithm of seismic moments. Seismic moments were obtained using the least-squares inversion (Text S2) per earthquakes. single and event averaged  $f_0$  and  $\Delta\tau$  are indicated by grey and red circles, respectively. Vertical error bars are the standard deviations to the different estimates. Linear fits to event averages are indicated by dashed black lines with slopes and standard deviations indicated in panel legends. The dotted curve in (a) is the fit assuming earthquake self-similarity (constant stress drop), i.e., a slope of  $-1/3$ .

Figure 1.

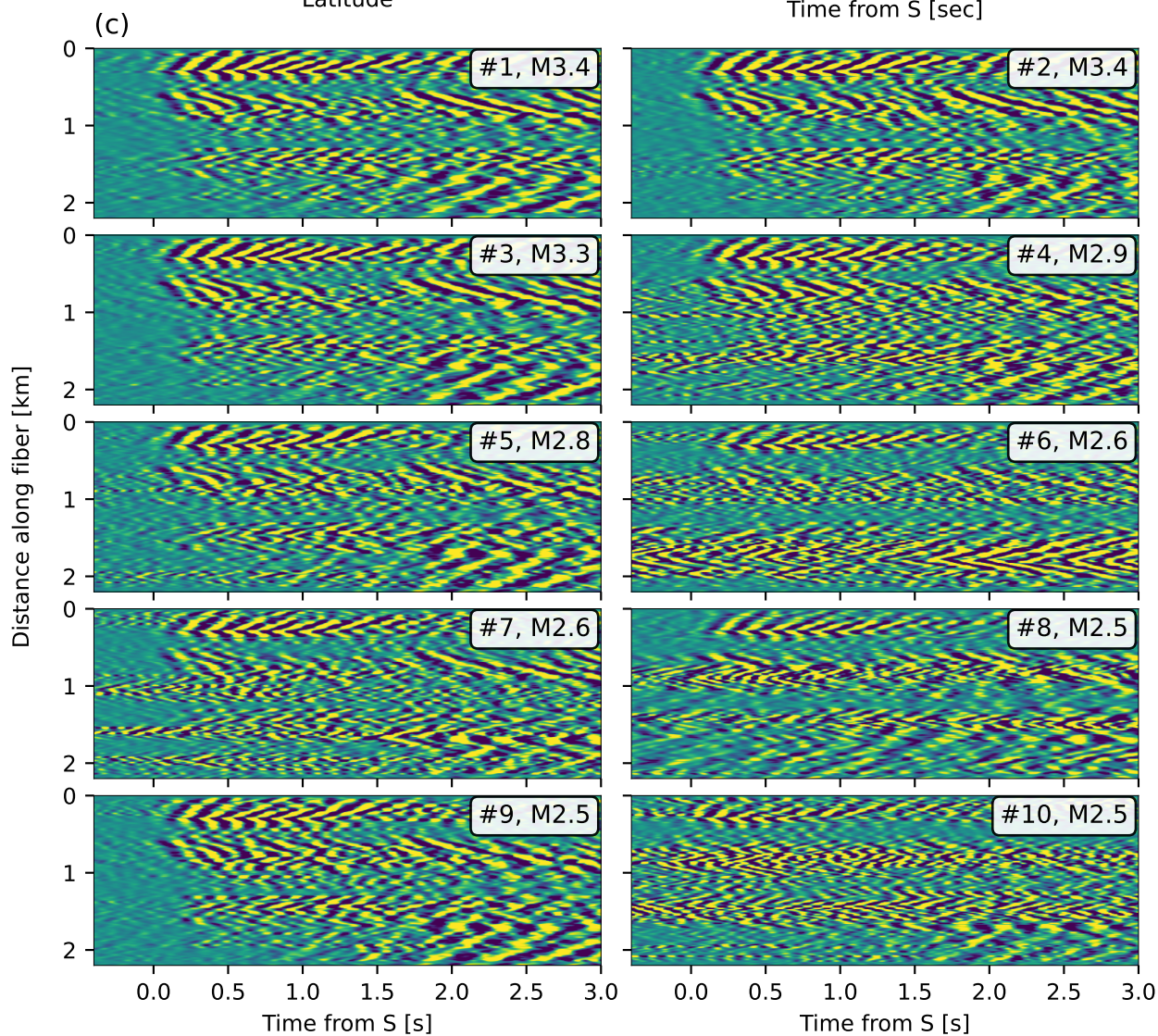
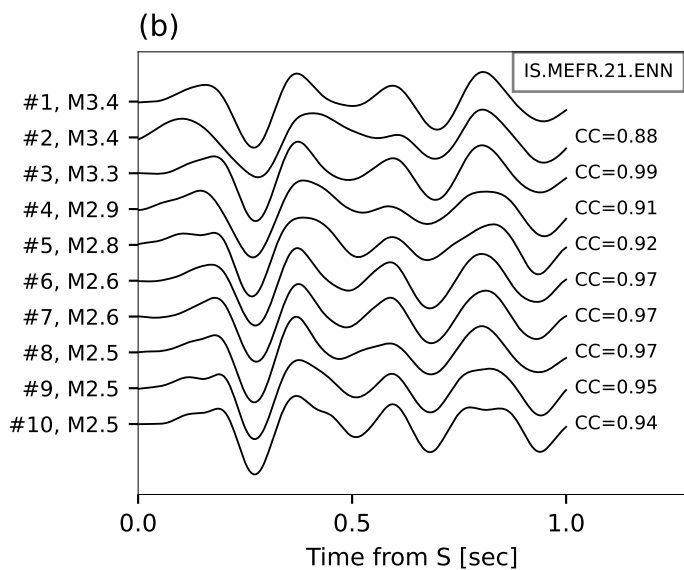
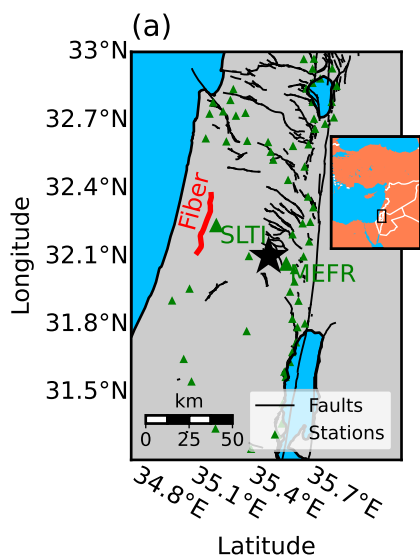


Figure 2.



— Spectrum — Resampled ---- Model fit

Stacked relative log amplitude

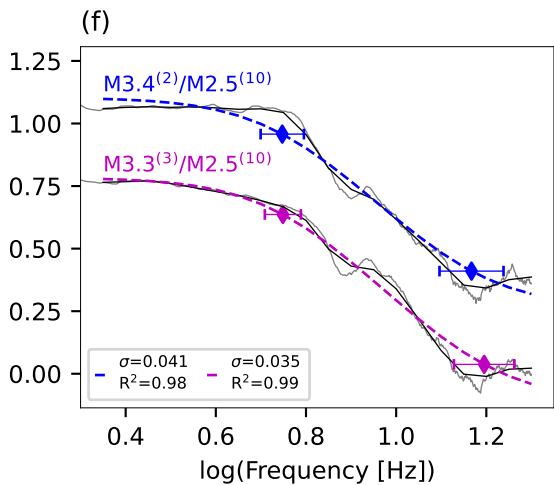
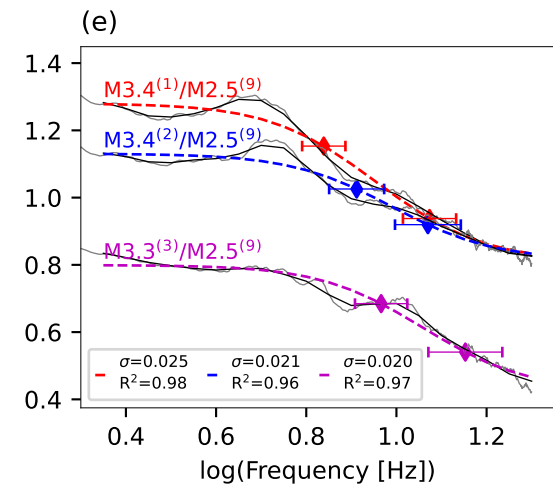
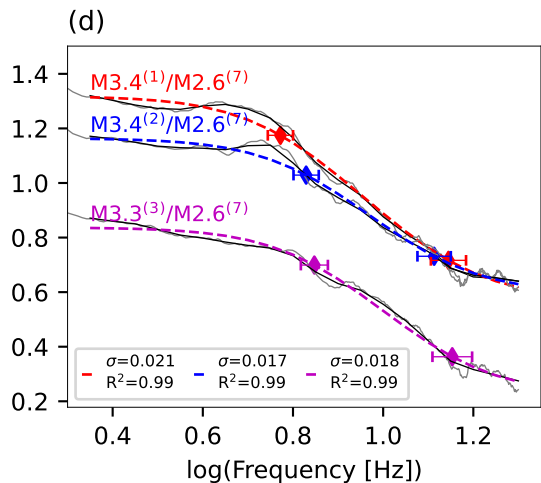
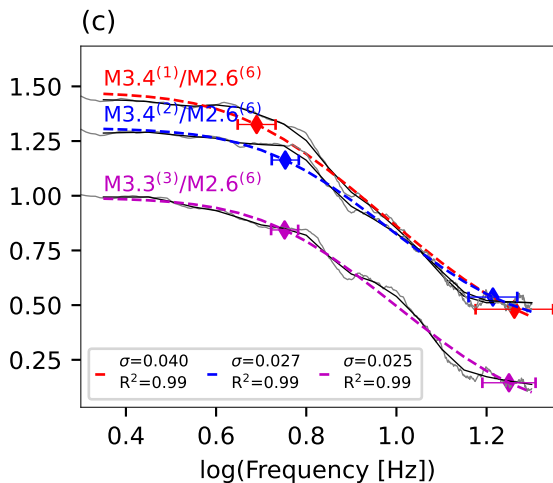
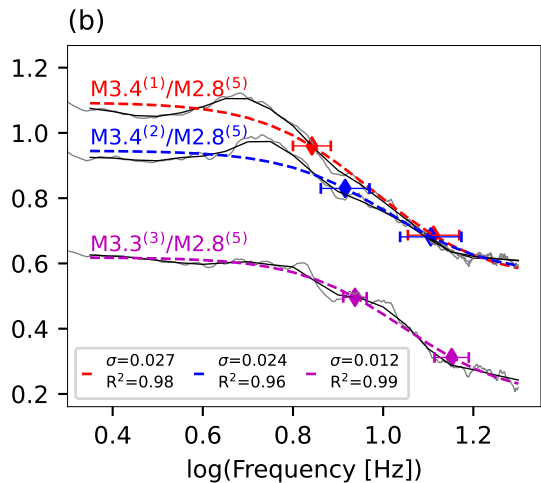
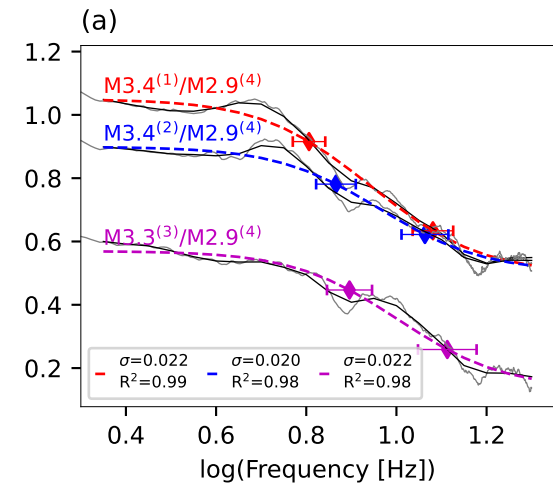
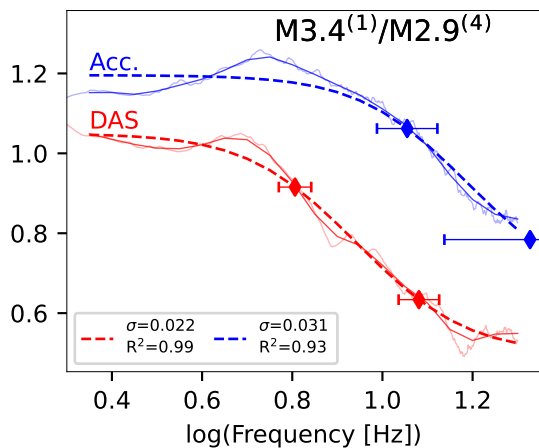


Figure 3.

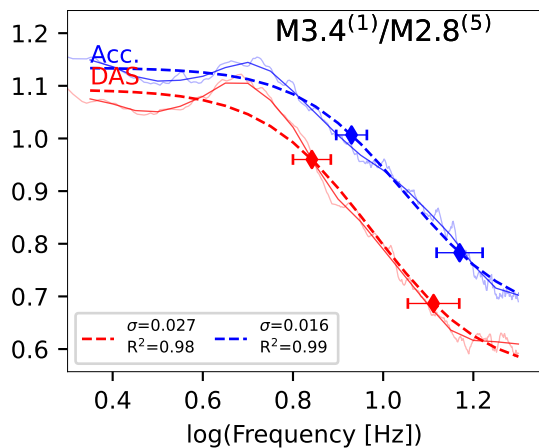
— Spectrum — Resampled ---- Model fit

Stacked relative log amplitude

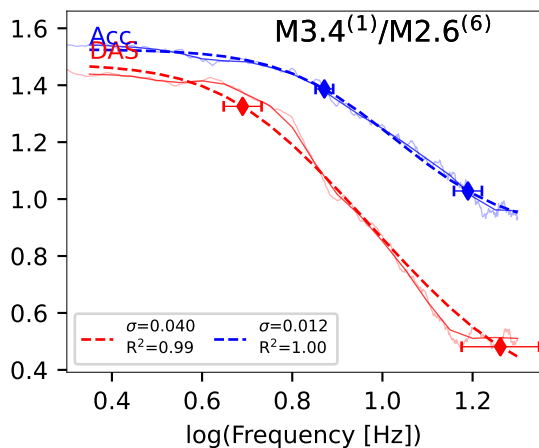
(a)



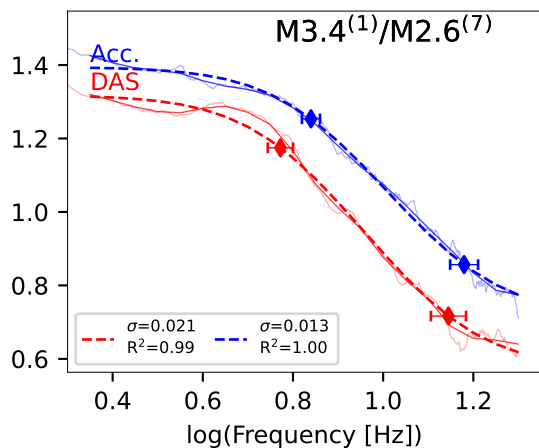
(b)



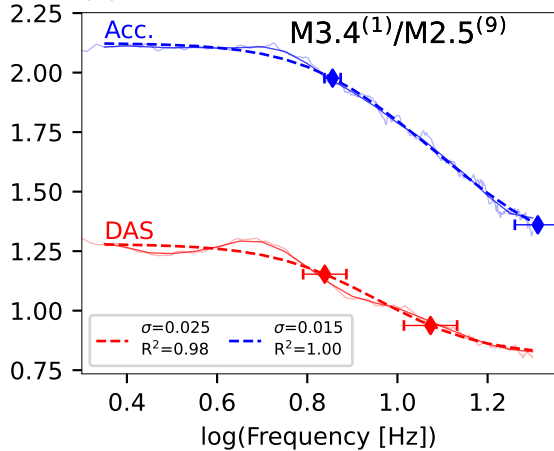
(c)



(d)



(e)



(f)

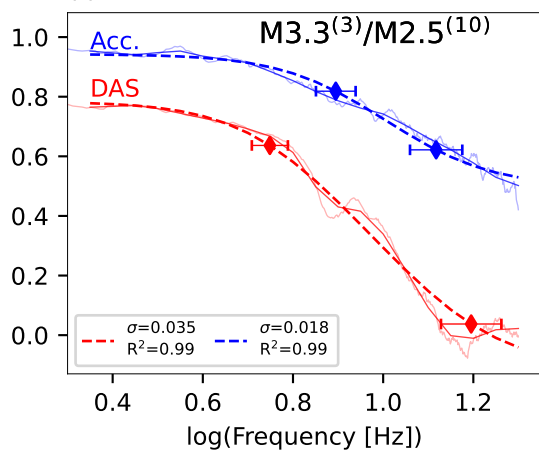
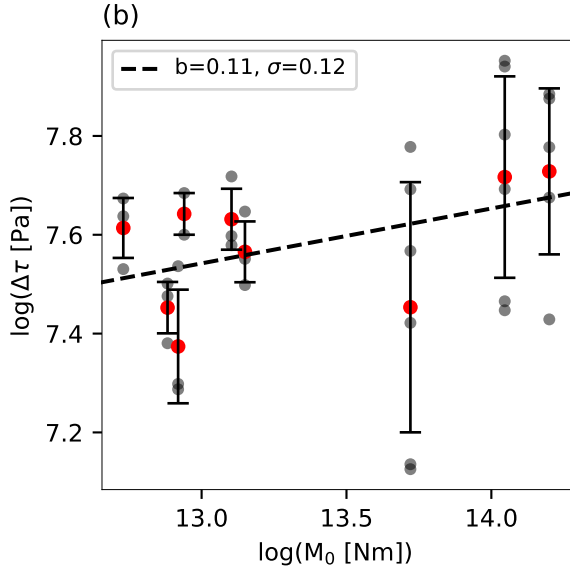
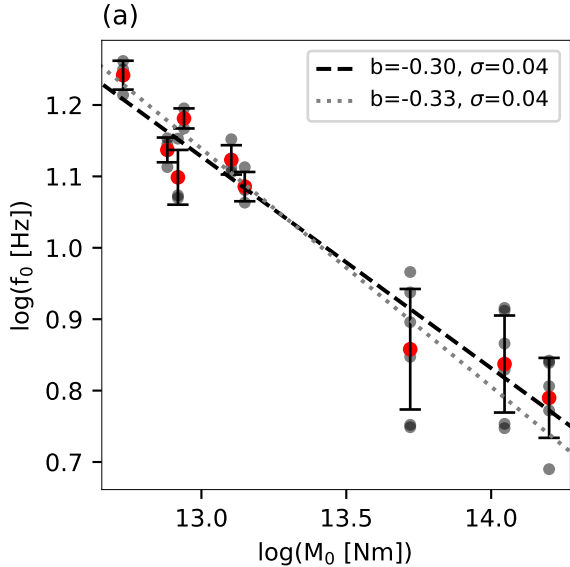


Figure 4.



1  
2  
3  
4  
5  
6

*Geophysical Research Letters*

Supporting Information for

**Accurate Magnitude and Stress Drop using the Spectral Ratios Method Applied to  
Distributed Acoustic Sensing**

Itzhak Lior

Institute of Earth Sciences, The Hebrew University, Jerusalem, Israel.

7 **Contents of this file**

8       Text S1 to S2  
9       Figures S1 to S4  
10      Tables S1

11 **Introduction**

12 This supplementary describes the derivation of the spectral ratios for DAS strain-rate  
13 data and the least-squares inversion for seismic moments. In addition, this file contains  
14 several supporting figures and a table containing earthquake metadata.

**Text S1.**

Recorded ground motions are a convolution between the source function  $\Omega_i$  (e.g., Equation 1) and the Green's function  $G_{ij}$ , where the latter describes wave propagation between earthquake  $i$  and recording station  $j$ , i.e., path, site and instrumental effects. In the frequency domain, ground accelerations may be written as:

$$A_{ij}(f, x) = (2\pi f)^2 \Omega_i(f) G_{ij}(f, x), \quad (S1)$$

where  $x$  is the spatial coordinate. To describe DAS recorded strain-rates  $\dot{\epsilon}_{ij}(f, x)$  using a source model (Equation 1), they need to be converted to ground motions (e.g., ground accelerations). This conversion is usually achieved using the apparent phase velocity recorded along the fiber's direction  $e$ ,  $C_{ij}^e(f, x)$ , which is a function of both frequency and location along the fiber (Lior, Sladen, Mercerat, et al., 2021):

$$\dot{\epsilon}_{ij}^e(f, x) = \frac{A_{ij}^e(f, x)}{C_{ij}^e(f, x)} \text{sinc}(k_z L/2) = \frac{(2\pi f)^2 \Omega_i(f) G_{ij}^e(f, x)}{C_{ij}^e(f, x)} \text{sinc}\left(\frac{\pi f L}{C_{ij}^e(f, x)}\right). \quad (S2)$$

The superscripts  $e$  denote quantities projected along the fiber's axis.  $C_{ij}^e(\omega, x)$  is a function of propagation direction (Mateeva et al., 2014) and media properties (Lior, Sladen, Rivet, et al., 2021) and as such, a function of  $G_{ij}^e$ , i.e.,  $C_{ij}^e(G_{ij}^e(\omega, x))$ . The  $\text{sinc}(k_z L/2)$  function should also be included for strain to ground motion conversion formulation. This function of gauge length, frequency and apparent velocity, represents the response of DAS recorded strain-rates which differ from point measured strain-rates. The transition in the above equation uses  $k_z = \frac{2\pi f}{C_{ij}^e(f, x)}$ . When taking the spectral ratios between two earthquakes ( $i = 1, 2$ ) recorded by the same fiber channel ( $j$ ), all Green's function dependent terms ( $G_{ij}^e$ ,  $C_{ij}^e$  and the  $\text{sinc}$  function) vanish:

$$\frac{\dot{\epsilon}_{1j}^e(\omega, x)}{\dot{\epsilon}_{2j}^e(\omega, x)} = \frac{\Omega_1(\omega)}{\Omega_2(\omega)} = \frac{\frac{\Omega_{01} U_{\phi\theta 1}}{\left[1 + \left(\frac{f}{f_{01}}\right)^{2\gamma}\right]^{1/\gamma}}}{\frac{\Omega_{02} U_{\phi\theta 2}}{\left[1 + \left(\frac{f}{f_{02}}\right)^{2\gamma}\right]^{1/\gamma}}} = \frac{M_{01} \left[1 + \left(\frac{f}{f_{02}}\right)^{2\gamma}\right]^{1/\gamma}}{M_{02} \left[1 + \left(\frac{f}{f_{01}}\right)^{2\gamma}\right]^{1/\gamma}}. \quad (S3)$$

The second equality above uses Equation (1) and the third equality uses  $\Omega_0 \propto \frac{M_0}{R}$ . Assuming that the earthquakes have the same mechanism,  $U_{\phi\theta i}$  also cancel.  $U_{\phi\theta i}$  can also be safely assumed to cancel regardless of mechanism if the analysis is done in the frequency domain and applied to coda waves recorded at multiple stations in a sufficient azimuthal range (e.g., Shearer et al., 2019). This result shows that the spectral ratios approach is directly applicable to DAS data and circumvents the need to convert strain-rates to ground motions.

## Text S2.

The fitting of Equation 3 to the spectral ratios of the 7 available earthquakes produced 12 estimates of  $\log(M_{01}/M_{02})$ . I treat this overdetermined problem as a linear inverse problem, that may be formulated as  $d = Gm$  where  $d$  is the data vector (the logarithms of moment ratios),  $m$  is the model (the logarithms of the seismic moments we want to obtain), and  $G$  is the model operator. Since only relative moments are available, at least one seismic moment needs to be constrained. I fixed the magnitude of the largest earthquake to its catalog value of 4.3 by adding an additional line and value to matrix  $G$  and vector  $d$ , respectively. The problem can be written explicitly as:

$$\begin{bmatrix} d_{1,4} \\ d_{1,5} \\ d_{1,6} \\ d_{1,7} \\ d_{1,9} \\ d_{2,4} \\ d_{2,5} \\ d_{2,6} \\ d_{2,7} \\ d_{2,9} \\ d_{2,10} \\ d_{3,4} \\ d_{3,5} \\ d_{3,6} \\ d_{3,7} \\ d_{3,9} \\ d_{3,10} \\ 14.2 \end{bmatrix} = \begin{bmatrix} 1 & 0 & 0 & -1 & 0 & 0 & 0 & 0 & 0 \\ 1 & 0 & 0 & 0 & -1 & 0 & 0 & 0 & 0 \\ 1 & 0 & 0 & 0 & 0 & -1 & 0 & 0 & 0 \\ 1 & 0 & 0 & 0 & 0 & 0 & -1 & 0 & 0 \\ 1 & 0 & 0 & 0 & 0 & 0 & 0 & -1 & 0 \\ 0 & 1 & 0 & -1 & 0 & 0 & 0 & 0 & 0 \\ 0 & 1 & 0 & 0 & -1 & 0 & 0 & 0 & 0 \\ 0 & 1 & 0 & 0 & 0 & -1 & 0 & 0 & 0 \\ 0 & 1 & 0 & 0 & 0 & 0 & -1 & 0 & 0 \\ 0 & 1 & 0 & 0 & 0 & 0 & 0 & -1 & 0 \\ 0 & 1 & 0 & 0 & 0 & 0 & 0 & 0 & -1 \\ 0 & 0 & 1 & -1 & 0 & 0 & 0 & 0 & 0 \\ 0 & 0 & 1 & 0 & -1 & 0 & 0 & 0 & 0 \\ 0 & 0 & 1 & 0 & 0 & -1 & 0 & 0 & 0 \\ 0 & 0 & 1 & 0 & 0 & 0 & -1 & 0 & 0 \\ 0 & 0 & 1 & 0 & 0 & 0 & 0 & -1 & 0 \\ 0 & 0 & 1 & 0 & 0 & 0 & 0 & 0 & -1 \\ 1 & 0 & 0 & 0 & 0 & 0 & 0 & 0 & 0 \end{bmatrix} \begin{bmatrix} \log(M_{0,1}) \\ \log(M_{0,2}) \\ \log(M_{0,3}) \\ \log(M_{0,4}) \\ \log(M_{0,5}) \\ \log(M_{0,6}) \\ \log(M_{0,7}) \\ \log(M_{0,9}) \\ \log(M_{0,10}) \end{bmatrix}, \quad (S4)$$

where the last value in  $d$  is the  $\log(M_0)$  (in  $Nm$ ) of the Mw 4.3 earthquake, and subscripts in  $d$  and  $m$  denote the earthquake numbers (Table S1). This problem is overdetermined and was solved by finding the Moore-Penrose generalized inverse of  $G$  via Python's Numpy linalg.pinv tool. To verify that a stable solution was obtained, I plotted the percentile change in the logarithms of moment ratios as a function of the initial logarithms of moment ratio (vector  $d$ ) for the 12 available observations. The changes are less than 0.2%, validating the stability of the inversion. Obtained magnitudes are specified in Table S1.



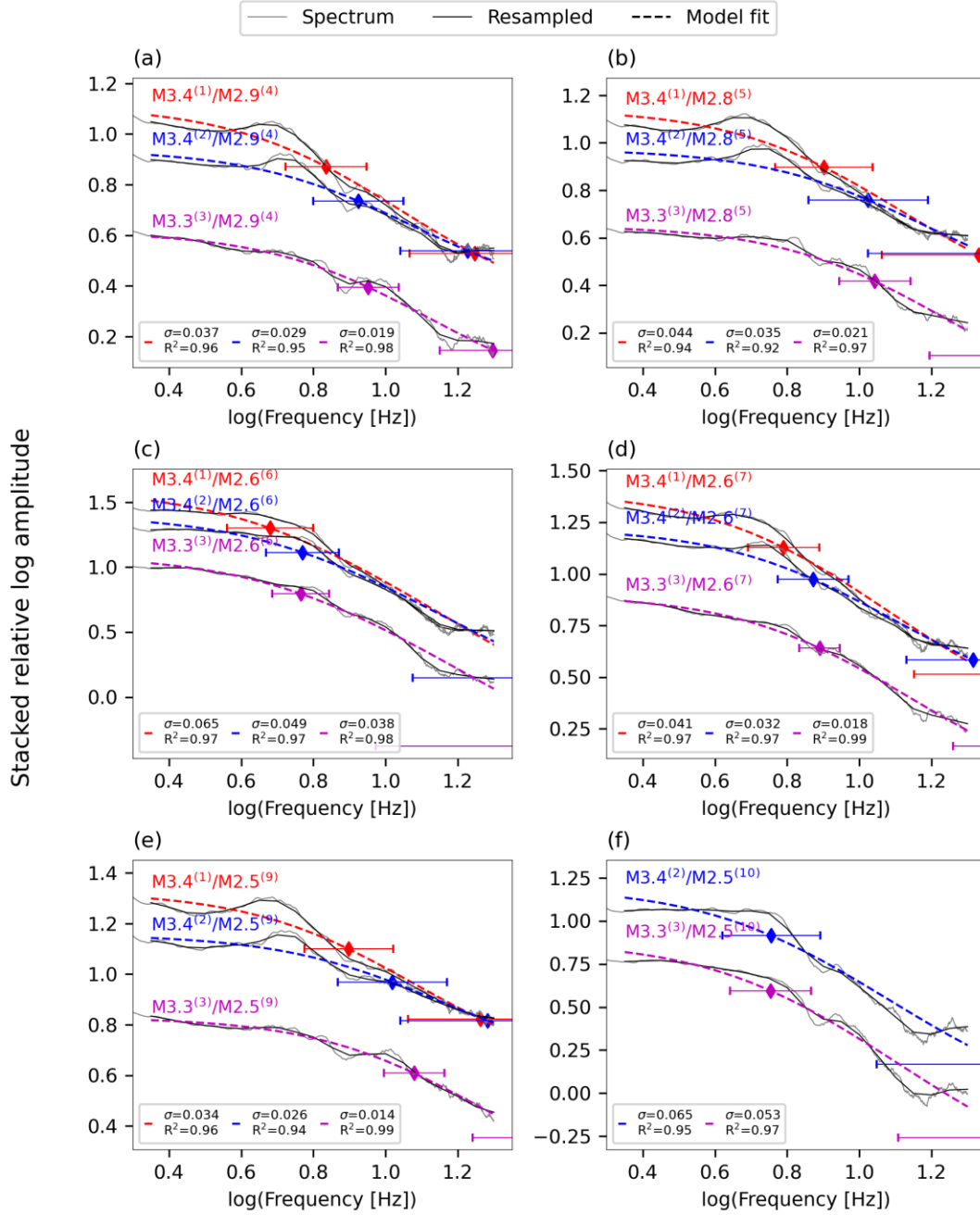
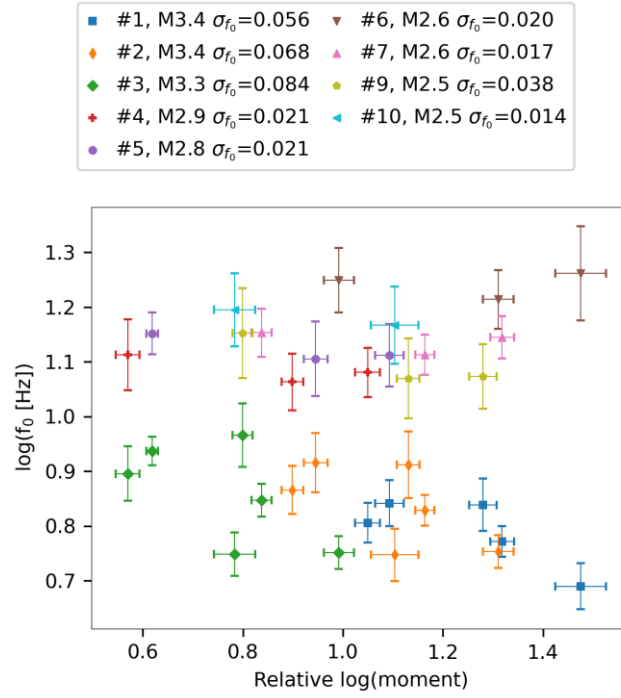
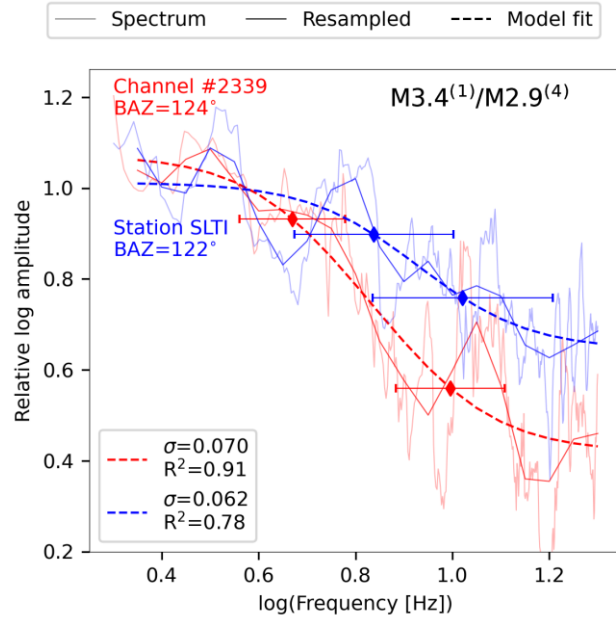


**Figure S1.** Spectral ratios and fits using the Brune ( $\gamma = 1$  in Equation 3) model for different earthquake pairs. Stacked spectral ratios, resampled ratios and model fits are indicated by thin grey curves, black curves, and dashed colored curves, respectively. Standard deviations and  $R^2$  are indicated in the panel legends, corner frequency uncertainties are indicated by horizontal error bars. Red, blue and magenta curves correspond to different larger earthquake while each panel shows a specific smaller earthquake. Earthquake magnitude and numbers (Table S1) are indicated near each curve.



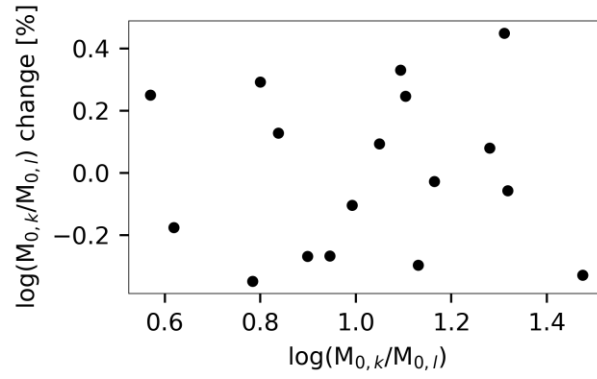
64

65 **Figure S2.**  $\log(f_0)$  as a function of  $\log(M_{01}/M_{02})$ , with associated error bars, for the fits to the  
66 Boatwright model in Figure 3. Different earthquakes are indicated by different colors and  
67 markers. The legend indicates the earthquake number, catalog magnitude (corresponding to  
68 Table S1) and standard deviation to earthquake specific  $\log(f_0)$  estimates.



69

70 **Figure S3.** Spectral ratios for magnitude 3.4 and 2.9 earthquakes using a single DAS channel  
 71 (#2339) and single accelerometer (station SLTI), located at a similar back azimuth (BAZ) from  
 72 the source location. DAS fits yield  $\log(M_{01}/M_{02}) = 1.07$ ,  $f_{01} = 4.67 \text{ Hz}$  and  $f_{02} = 9.9 \text{ Hz}$   
 73 and the accelerometer yields  $\log(M_{01}/M_{02}) = 1.01$ ,  $f_{01} = 6.88 \text{ Hz}$  and  $f_{02} = 10.5 \text{ Hz}$ .  
 74 Spectral ratios, resampled ratios and model fits are indicated by thin curves, thick curves, and  
 75 dashed curves, respectively. Standard deviations and  $R^2$  are indicated in the panel legend,  
 76 corner frequency uncertainties are indicated by horizontal error bars. Red and blue curves  
 77 correspond to DAS and accelerometer spectral ratios, respectively. Earthquake magnitude and  
 78 numbers (Table S1) are indicated in the figure.



79

80 **Figure S4.** Percentile change in the logarithms of moment ratios as a function of the  
81 logarithm of moment ratio. The former is calculated using specific log-moments obtained  
82 following the least-squares inversion (Text S2) and the latter are obtained via model fitting to  
83 stacked spectral ratios. Indices  $k$  and  $l$  denote different earthquake combinations.

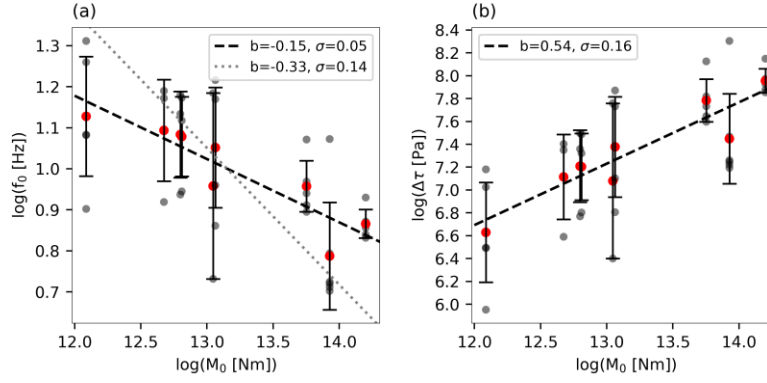
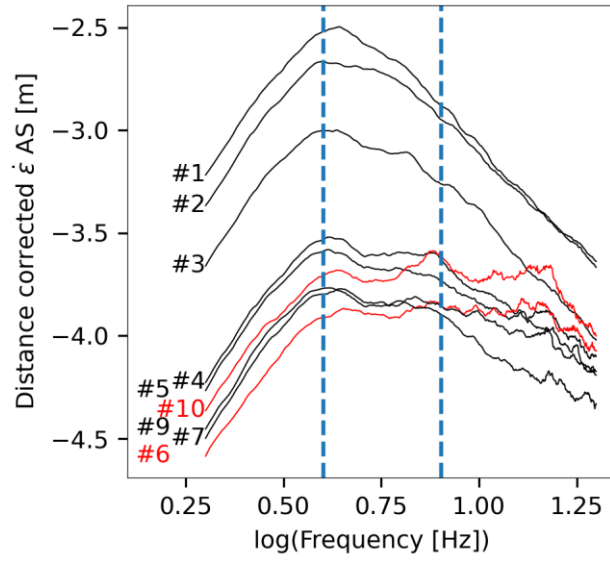


**Figure S5.** The logarithms of (a) corner frequencies and (b) stress drops as functions of the logarithm of seismic moments for accelerometer data. Seismic moments were obtained using the least-squares inversion (Text S2) per earthquakes. Fit-specific and event averaged  $f_0$  and  $\Delta\tau$  are indicated by grey and red circles, respectively. Vertical error bars are the standard deviations to the different estimates. Linear fits to event averages are indicated by dashed black lines with slopes and standard deviations indicated in panel legends. The dotted curve in (a) is the fit assuming earthquake self-similarity (constant stress drop), i.e., a slope of -1/3.



92

93 **Figure S6.** Earthquake strain-rate amplitude spectra stacked using high SNR amplitudes along  
 94 the fiber. Earthquakes #3 to #10 exhibit a noticeable trough between 4 and 8 Hz (vertical  
 95 dashed lines) while earthquakes #1 and #2 do not. Earthquake #8 is not shown.

	Origin Time (UTC)	Magnitude	Location (Latitude, Longitude, depth [km])	Geometric mean $f_0$ , Hz	Parameters following least squares inversion		
					$\log(M_0, Nm)$	Moment magnitude	Geometric mean $\Delta\tau$ , Pa
1	2023-02-07 21:14:28	Mw 3.4	32.103, 35.301, 12	6.16	14.2	3.4	53.49
2	2023-02-08 14:58:40	MI 3.4	32.109, 35.315, 1	6.87	14.05	3.3	52.09
3	2023-02-18 04:09:06	MI 3.3	32.104, 35.321, 1	7.21	13.72	3.08	28.4
4	2023-02-08 03:03:00	MI 2.9	32.11, 35.308, 2	12.18	13.15	2.70	36.77
5	2023-02-08 16:41:07	MI 2.8	32.116, 35.321, 4	13.28	13.10	2.67	42.8
6	2023-02-08 15:07:41	MI 2.6	32.097, 35.323, 3	17.45	12.73	2.42	41.1
7	2023-03-01 20:20:59	MI 2.6	32.100, 35.314, 5	13.71	12.88	2.52	28.35
8	2023-02-07 23:14:37	MI 2.5	32.094, 35.308, 1	--	--	--	--
9	2023-02-07 22:07:31	MI 2.5	32.110, 35.341, 5	12.55	12.92	2.55	23.66
10	2023-03-07 07:20:07	MI 2.5	32.096, 35.339, 5	15.18	12.94	2.56	43.88

**Table S1.** Earthquakes used in this study. Stress drops were calculated using the Madariaga (1976) model, for Brune (1970) stress drops, divide by 5.5. Data from the Geological Survey of Israel: <https://eq.gsi.gov.il/en/indexEn.php>, where the focal mechanism of earthquake #1 is also available. Earthquake numbering matches that of Figures 1, S2 and 3.